ELSEVIER

Contents lists available at ScienceDirect

Additive Manufacturing

journal homepage: www.elsevier.com/locate/addma





Recurrence network analysis of design-quality interactions in additive manufacturing

Ruimin Chen^a, Prahalada Rao^b, Yan Lu^c, Edward W. Reutzel^d, Hui Yang^{a,*}

- ^a The Harold and Inge Marcus Department of Industrial and Manufacturing Engineering, The Pennsylvania State University, University Park, PA, USA
- ^b Mechanical and Materials Engineering, University of Nebraska-Lincoln, Lincoln, NE, USA
- ^c Systems Integration Division, National Institute of Standards and Technology, Gaithersburg, MA, USA
- ^d Applied Research Laboratory, The Pennsylvania State University, University Park, PA, USA

ARTICLE INFO

Keywords: Additive manufacturing Recurrence network Design of experiments Engineering design Quality control Thin-wall structure

ABSTRACT

Powder bed fusion (PBF) additive manufacturing (AM) provides a great level of flexibility in the design-driven build of metal products. However, the more complex the design, the more difficult it becomes to control the quality of AM builds. The quality challenge persistently hampers the widespread application of AM technology. Advanced imaging (e.g., X-ray computed tomography scans and high-resolution optical images) has been increasingly explored to enhance the visibility of information and improve the AM quality control. Realizing the full potential of imaging data depends on the advent of information processing methodologies for the analysis of design-quality interactions. This paper presents a design of AM experiment to investigate how design parameters (e.g., build orientation, thin-wall width, thin-wall height, and contour space) interact with quality characteristics in thin-wall builds. Note that the build orientation refers to the position of thin-walls in relation to the recoating direction on the plate, and the contour space indicates the width between rectangle hatches. First, we develop a novel generalized recurrence network (GRN) to represent the AM spatial image data. Then, GRN quantifiers, namely degree, betweenness, pagerank, closeness, and eigenvector centralities, are extracted to characterize the quality of layerwise builds. Further, we establish a regression model to predict how the design complexity impacts GRN behaviors in each layer of thin-wall builds. Experimental results show that network features are sensitive to build orientations, width, height, and contour space under the significant level $\alpha = 0.05$. Thin-walls with the width bigger than 0.1 mm printed under orientation 0° are found to yield better quality compared to 60° and 90°. Also, thin-walls build with orientation 60° are more sensitive to the changes in contour space compare to the other two orientations. As a result, the orientation 60° should be avoided while printing thin-wall structures. The proposed design-quality analysis shows great potential to optimize engineering design and enhance the quality of PBF-AM builds.

1. Introduction

Powder bed fusion (PBF) additive manufacturing (AM) provides an unprecedented opportunity to produce metal builds with complex geometries layer by layer directly from digital designs. In contrast with conventional subtractive manufacturing, AM technology offers a higher degree of design freedom and avoids extra tooling costs [1]. Therefore, design constraints in conventional subtractive manufacturing (i.e., design for manufacturing) are lessened by this new technology. In other words, PBF-AM enables a new paradigm of "manufacturing for design" to fabricate the complex design in a layer-by-layer fashion [2]. Consequently, the rapid development of digital manufacturing and material

science in recent years fuels the widespread applications of AM in many industries such as aerospace [3] and healthcare [4].

However, a higher level of design complexity tends to degrade the quality of final PBF-AM builds and lower the repeatability of the process [5]. Advanced imaging (e.g., X-ray computed tomography scans and high-resolution optical images) is increasingly utilized to cope with design complexity and enhance the information visibility for quality assessment [6]. However, advanced AM imaging technologies bring complex-structured and high-dimensional spatial data (i.e., a large number of pixels that are spatially correlated in each layerwise image of an AM build). There is a dire need to develop new analytical methodologies that realize the full potential of imaging data for the analysis of

E-mail address: huy25@psu.edu (H. Yang).

^{*} Corresponding author.

design-quality interactions.

Recurrence plot (RP) and recurrence quantification analysis (RQA) are widely used to graphically represent recurrence dynamics and quantify recurrence patterns of nonlinear time series analysis in complex manufacturing systems. However, traditional RP and RQA tend to be limited in the ability to handle high-dimensional spatial data. To delineate recurrence dynamics in the spatial data, prior efforts have been made to extend the recurrence plot to a four-dimensional hyperspace [7]. However, this conventional method can only visualize the recurrence patterns in the reduced-dimension space and is rather limited in the ability to provide a complete picture of recurrence patterns in AM spatial imaging data. New analytical methodologies are needed to (1) characterize recurrence behaviors and patterns in AM spatial data; (2) measure and quantify the recurrence features; and (3) analyze the relationship between the extracted features and the quality of AM builds.

This study presents our experimental studies on PBF-AM, as well as the analysis of imaging data to investigate the relationship between design parameters and quality characteristics through a recurrence network approach. The proposed methodology, namely the generalized recurrence network (GRN) approach enables (1) effective visualization of complex spatial patterns in AM images that overcomes the "curse of dimensionality" problem in the traditional RP methodologies; (2) the use of network theory to characterize and quantify recurrence properties, thereby reducing high-dimensional image profiles into a lower-dimensionality set of quantifiers; and (3) the design of experiments to select important features, and predict how the design complexity impacts network characteristics in each layer of thin-wall builds.

The proposed methodology is evaluated and validated with simulation and real-world case studies of thin-wall structures fabricated by the PBF-AM. The simulation study is aimed at evaluating the effectiveness of GRN to characterize layerwise imaging data as well as testing the significance of quantifiers with defect variations. In the real-world case study, we conduct a series of experiments to fabricate thin-wall structures by varying the levels of design parameters such as build orientation (i.e., the planar inclination of thin-walls in the X-Y plane with respect to the recoater blade), thin-wall width, thin-wall height, and contour space (see Section 4). Thin-wall structures are commonly utilized in heat exchangers to increase the efficiency of thermal transfer and reduce the material consumption. However, fabricating thin-wall structures is a challenging task for PBF-AM. Therefore, a better understanding the design-quality interaction is urgently needed. As illustrated in Fig. 1, thin-walls may collapse, contain pores and lack-of-fusion defects, or have structural inconsistency. A total of three thin-wall builds were made using the PBF-AM. A post-build inspection on the parts was conducted with X-ray computed tomography (XCT). Then, we registered the XCT images layer-by-layer with the sliced computer-aided design (CAD) files to delineate the region of interest (ROI) and then measure qualityrelated features. These network features characterize the defect patterns (i.e., inversely proportional to the quality level) in each layer, which are then used to track the variation of quality across layers so as to detect impending failures in the layers of a thin-wall. Lastly, we performed an analysis of variance (ANOVA) analysis to select important features then constructed a regression model to predict how design complexity impacts network characteristics in each layer of thin-wall structures. Experimental results show that the build quality is sensitive to build orientation, thin-wall width, thin-wall height, and contour space.

The rest of the paper is organized as follows: Section 2 reviews the related literature on AM design studies and provides the research background in recurrence analysis. Section 3 presents the experimental setup and GRN analysis of spatial data. The experimental results are provided in Section 4. Section 5 concludes this study.

2. Research background

2.1. Quality control and design parameters in PBF-AM

The quality of an AM build is impacted by feedstock materials, machine environment, process settings, and design complexity. Our prior studies concentrated on the impact of process and machine settings (e.g., scanning velocity, laser power, and hatch spacing) on the builds quality [8,9]. Furthermore, we developed a Markov decision process model to sequentially optimize the quality of AM builds [10,11]. This paper specifically focuses on the interactions between design parameters and quality characteristics. Several prior works have been done to study the builds of thin-wall structures when the design parameters are varied. Thomas [12] reported that walls thinner than 0.4 mm are difficult to build based on experimental studies on an MCP Realizer 250 SLM machine. Dunbar et al. [13] tried different process settings (i.e., laser power, velocity, and scan type) to test the limits of thin, metallic components using PBF-AM. They found that thin-walls fabricated with the orientation of 90° are consistently thicker than the thin-wall built with the orientation 45°. Kranz et al. [14] conducted experiments on the EOS 270xt, and showed that it is possible to manufacture thin-wall structures made of TiAl6V4 in all the examined orientations (i.e.,0°, 45°, 90°, 135°, and 180°) at a minimum thickness from 0.4 mm. Thin-walls of 0.3 mm were only successfully printed under orientation 30°; however, the highest deviation is also observed at the orientation of 30°.

Gaikwad et al. [15] extracted statistical features (i.e., thickness, density, edge smoothness, and discontinuity) from imaging data to quantify the build quality, and further leveraged deep learning for real-time flaw detection. Our prior work has also studied the interaction between design complexity and edge roughness [16]. Note that the edge roughness is defined as the geometric deviation of thin-wall boundaries between the sliced CAD file and the registered XCT scan. However, the calculated edge roughness is treated as one-dimensional time series data and does not have a high-dimensional structure with geometric information. Few, if any, previous works have leveraged GRN analysis of imaging data to study interactions between design parameters and the quality of PBF final builds. AM imaging provides spatial data which includes both geographical coordinates and pixel intensity characteristics. Therefore, new analytical methodologies are urgently needed to

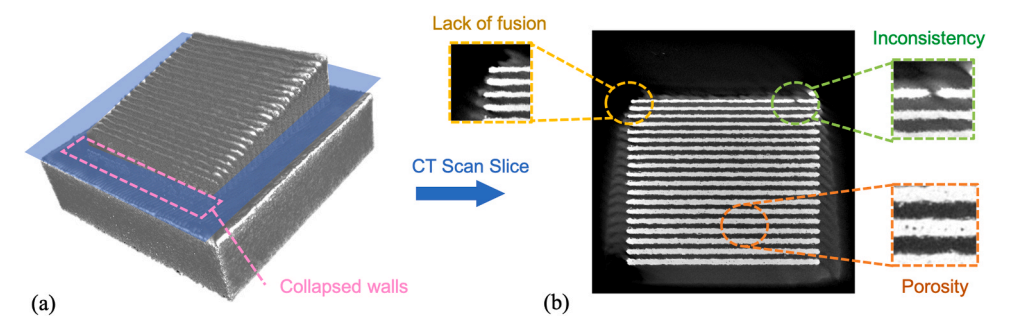


Fig. 1. (a) XCT scan of the thin-wall build in orientation 0° ; (b) a slice of XCT scan from the 103^{th} layer of 0° build with quality issues such as collapsed walls, lack of fusion, edge inconsistency, and porosity.

handle AM spatial data and extract useful information to analyze the design-quality interactions.

2.2. Recurrence analysis and network theory

Recurrence is a fundamental property that commonly exists in complex systems. For example, RQA provides an effective tool to analyze acoustic emission signals and extract features to estimate surface roughness of metal cutting [17]. Poincare recurrence theorem shows that the trajectory of a dynamical system will eventually reappear in the ε -neighborhood of former states [18]. Eckmann et al. [19] introduced a graphical tool, namely RP, to visualize recurrence patterns of dynamical systems in 1987. RP characterizes the proximity of two states using the Heaviside function Θ , then obtains the topological relationships in the state spaces as a two-dimensional recurrence plot:

$$\mathbf{R}_{p,q} = \Theta(\varepsilon - \parallel \mathbf{s}_p - \mathbf{s}_q \parallel) \mathbf{s}_p, \mathbf{s}_q \in \mathbb{R}^m$$
 (1)

where $\mathbf{R}_{p,q}$ is the recurrence matrix \mathbf{R} , \mathbf{s}_p and \mathbf{s}_q are two states, and ε is a threshold. Mutual information and the false nearest neighbor are commonly used to select optimal delay and determine the embedding dimension for state-space reconstruction from time series. Mutual information quantifies both linear and nonlinear interdependence in the time series, and the optimal dimension is determined by varying the dimensionality and comparing the behavior of false nearest neighbors [20]. Zbilut and Webber [21] proposed RQA to extract statistical features from small-structures in the RP to understand the dynamical properties of complex systems. Yang and Chen [22] considered different types of recurrences in the state space and extended the conventional RQA to heterogeneous recurrence quantification analysis (HRQA). The HRQA has been widely applied in the manufacturing domain [23,24] as well as the healthcare area [25,26].

However, RP is limited in the ability to handle high-dimensional and geometric spatial data. Marwan et al. [7] extended the one-dimensional RP framework to high-dimensional spatial data:

$$\mathbf{R}(\mathbf{x}_p, \mathbf{x}_q) = \Theta(\varepsilon - || \mathbf{s}(\mathbf{x}_p) - \mathbf{s}(\mathbf{x}_q) ||) \quad \mathbf{s}(\mathbf{x}_p), \mathbf{s}(\mathbf{x}_q) \in \mathbb{R}^m$$
 (2)

where $\mathbf{s}(\mathbf{x}_p)$ and $\mathbf{s}(\mathbf{x}_q)$ are the states (i.e., pixel intensity), \mathbf{x}_p and \mathbf{x}_q denotes the spatial locations. If the intensity differences between two pixels is less than threshold ε , there exists a recurrence. However, only limited information about the recurrence behavior can be visualized. Let's denote the spatial reference (i.e., location information) as $\mathbf{x}=(x_1,x_2,\ldots,x_d)$ with d dimensions, and the attribute set as $\mathbf{a}=(a_1,a_2,\ldots,a_m)$ with m dimensions. A pixel p in a two-dimensional image contains the location $\mathbf{x}_p=(x_1^{(p)},x_2^{(p)})$ and attribute $\mathbf{a}_p=(a_R^{(p)},a_G^{(p)},a_B^{(p)})$. Then, a two-dimensional image will generate a four-dimensional RP $\mathbf{R}(\mathbf{x}_p,\mathbf{x}_q)=\mathbf{R}_{x_1^{(p)},x_2^{(p)},x_1^{(q)},x_2^{(q)}}$. However, only three out of four dimensions can be selected for the visualization in the three-dimensional coordinate system. It will be even more challenging to visualize three-dimensional imaging data which generates an RP of six dimensions $\mathbf{R}(\mathbf{x}_p,\mathbf{x}_q)=\mathbf{R}_{x_1^{(p)},x_2^{(p)},x_3^{(q)},x_1^{(q)},x_2^{(q)},x_3^{(q)}}$.

Further, Yang et al. [20,27] introduced a recurrence network for nonlinear time series analysis. Network nodes represent the states and edges denote the recurrence relationship.

$$\mathbf{A}_{p,q} = \boldsymbol{\Theta} \big(\boldsymbol{\varepsilon} - \parallel \mathbf{s}(\mathbf{x}_p) - \mathbf{s}(\mathbf{x}_q) \parallel \big) - \boldsymbol{\Delta}_{p,q} \quad \mathbf{s}(\mathbf{x}_p), \mathbf{s}(\mathbf{x}_q) \in \mathbb{R}^m$$
 (3)

where ε denotes the recurrence threshold, $\mathbf{A}_{p,q}$ is the adjacency matrix, $\Delta_{p,q}$ is the Kronecker delta, which prevents the self-loop in the recurrence network. However, the proposed recurrence network is designed for time series data, and cannot be utilized for spatial data directly. In this work, we leverage network theory to investigate the recurrence behavior of spatial data, further characterize and quantify spatial characteristics through network statistics.

3. Research methodology

This paper presents the analysis of design-quality interactions in the PBF-AM process. As shown in Fig. 2 (a), a total of three builds were fabricated, each differing in build direction (i.e., their planar inclination in the X-Y plane with respect to the recoater blade). We performed a post-build inspection through XCT. As shown in Fig. 2 (b), a shape-to-image registration is conducted between XCT images and layerwise CAD images. Next, we leveraged a GRN analysis to characterize and quantify the layerwise imaging data. Finally, we performed an ANOVA analysis to select important features and established a regression model to predict how the design complexity impacts the network behaviors in each layer of thin-wall builds.

3.1. Experimental setup

In this experiment, thin-wall parts were built from Spherical ASTM B348 Grade 23 Ti-6Al-4V powder with a size distribution of 14-45 µm on an EOS M280 PBF machine. As shown in Fig. 3, thin-wall parts are built vertically with a layer thickness of 60 µm in three orientations (i. e., 0°, 60°, and 90°) with respect to the travel direction of recoater blade (i.e., indicated by the arrow on each part). Standard EOS M280 processing parameters for 60 micron layers were complyed. Each thin-wall build consists of 25 thin-walls built on a platform of size $15 \text{ mm} \times 15 \text{ mm} \times 55 \text{ mm}$. The width of thin-walls increases from 0.06 mm, with a step size of 0.01 mm, to 0.3 mm. Also, two thin-walls are separated with a constant distance of 0.3 mm. It is worth mentioning that the height/width ratio of each thin-wall is 10. In other words, if the width of a thin-wall is 0.3 mm, then the height is set to be 3.0 mm. Contour space is defined as the width between rectangle hatches indicated by the pink arrpw in Fig. 3 (d). Table 1 shows the variation of contour spaces within thin-wall 1 to thin-wall 25. The distance between contours is 0.244 mm for thin wall 1, and decreases from thin-wall 1-24 (0.011 mm). Post build XCT data are obtained on General Electric V|tome|X system with a voxel size of 15 μm³.

3.2. Image registration

Image registration helps delineate the correspondence of ROIs between two images (i.e., a moving image and a fixed image) using a common coordinate system. Note that this paper focuses on the analysis of design-quality interactions and does not preclude others to use a different registration approach. We used a standard registration process with four components, namely similarity metric, optimizer, moving transformation, and interpolator. The similarity metric is aimed at evaluating the accuracy of image registration, which takes two images (i.e., the moving image and the fixed image) and returns a scalar value that measures the similarity between two images. Fig. 4 illustrates this iterative process and flow chart of image registration.

The mean square differences (\mathcal{D}) is used to define the similarity metric between a fixed image F and a transformed image M' as:

$$\mathscr{D}(F, M') = \frac{1}{N} \sum_{p=1}^{N} ||F(p) - M'(p)||^2 \quad \forall \, p \in F \cap M'$$
 (4)

where N represents the number of pixels in each image, F(p) shows the intensity of pixel p in the fixed image, M'(p) denotes intensity of pixel p in the transformed image.

$$M' = T(M) (5)$$

where M is the moving image, and T is the transformation function. The optimization problem is formulated as:

$$\operatorname{argmin} \mathscr{D}(F, M') \tag{6}$$

The gradient descent method is utilized to iteratively update T and

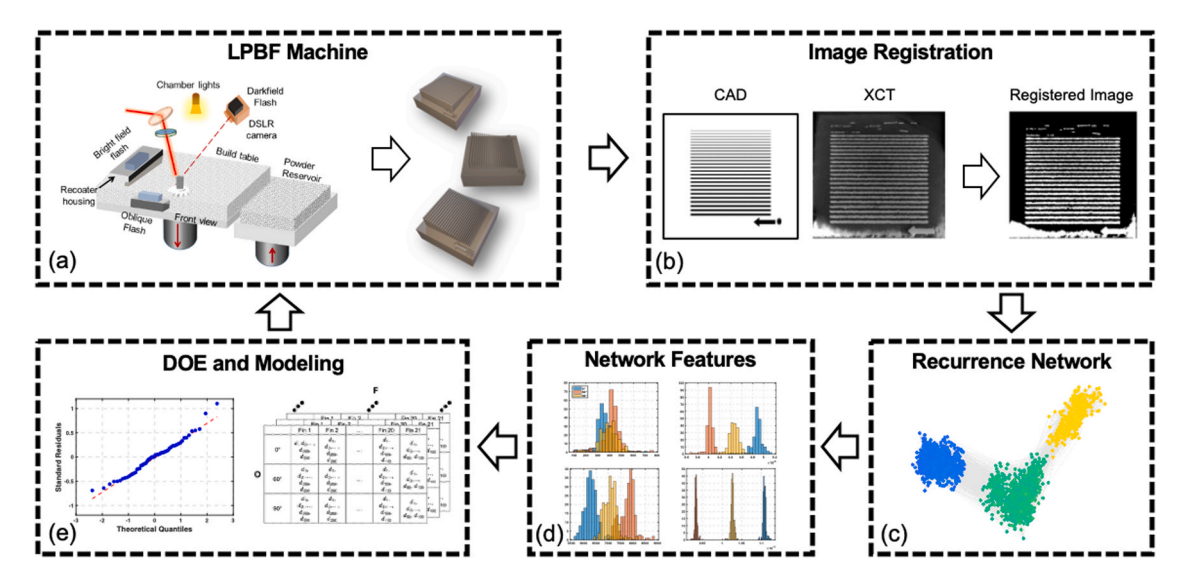


Fig. 2. The flow chart of research methodology.

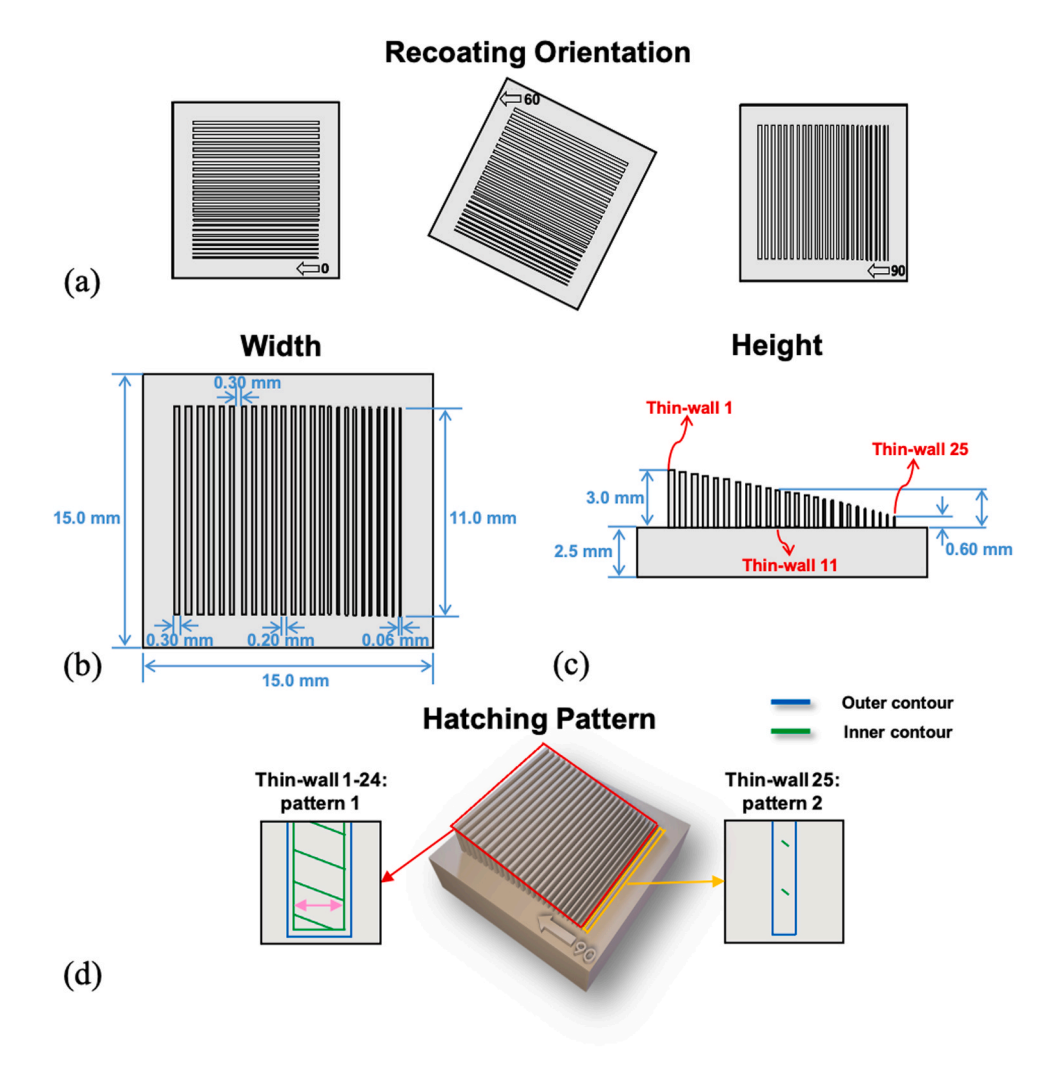


Fig. 3. (a) The orientation of thin-wall parts, (b) the top view of the CAD model, (c) the side view of the CAD model, and (d) the hatching patterns of the thin-walls. The pink arrow indicates the contour space. The blue and green solid lines represent outer and inner rectangle paths, respectively. (For interpretation of the references to color in this figure legend, the reader is referred to the web version of this article.)

Table 1The variations of contour spaces within contour from thin-wall 1 to thin-wall 25.

Thin-wall number	W_h mm								
1	0.244	6	0.190	11	0.142	16	0.092	21	0.045
2	0.234	7	0.183	12	0.136	17	0.082	22	0.033
3	0.220	8	0.167	13	0.125	18	0.076	23	0.022
4	0.208	9	0.159	14	0.114	19	0.059	24	0.011
5	0.198	10	0.154	15	0.102	20	0.049	25	N/A

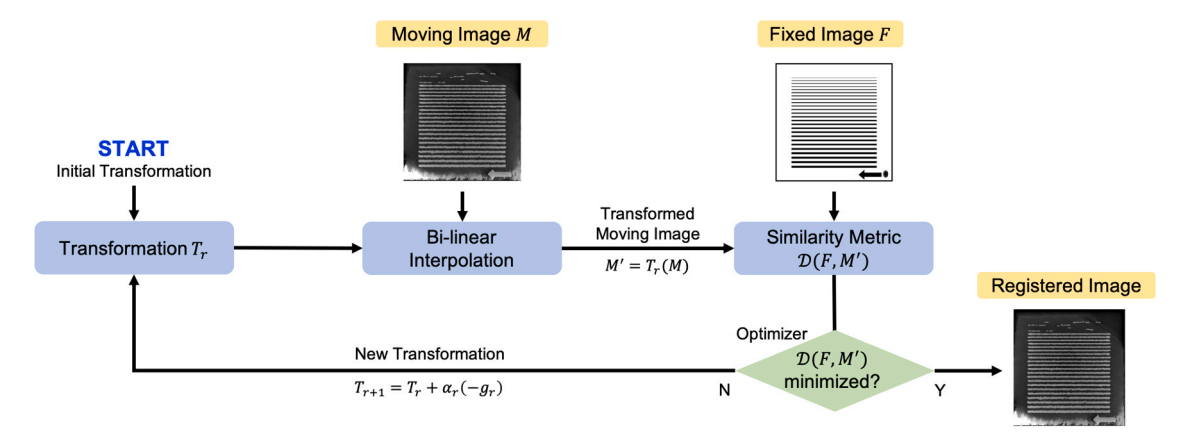


Fig. 4. The flow chart of image registration.

search for the minimum value of \mathcal{D} :

$$T_{r+1} = T_r + a_r(-g_r) (7)$$

where $a_r > 0$ is the step size at iteration r, g_r is the gradient vector of \mathcal{D} . Then, we isolate the region of interest (ROI) (i.e., each thin-wall) from the powder area in registered images. The extracted ROIs are used for the GRN analysis in the next session.

3.3. Recurrence network analysis of spatial data

Spatial data contains both spatial locations and intensity values of pixels. The traditional recurrence analysis is limited in the ability to analyze high-dimensional spatial data. Here, we propose a GRN analysis method, which accounts for both spatial closeness and pixel similarity. As discussed in Section 2, let's denote spatial reference as $\mathbf{x}=(x_1,x_2,\ldots,x_d)$, and attribute information as $\mathbf{a}=(a_1,a_2,\ldots,a_m)$, where d and m are the dimensions, respectively. For the pixel p in a two-dimensional image, $\mathbf{x}_p=(x_1^{(p)},x_2^{(p)})$ and $\mathbf{a}_p=(a_R^{(p)},a_G^{(p)},a_B^{(p)})$. For a 3D voxel q, $\mathbf{x}_q=(x_1^{(q)},x_2^{(q)},x_3^{(q)})$ and $\mathbf{a}_q=(a_R^{(q)},a_G^{(q)},a_B^{(q)})$. The edge weight of a recurrence network is formulated as:

$$w_{p,q} = I_{p,q} \times D_{p,q} \tag{8}$$

where the intensity similarity $I_{p,q}$ (i.e., the closeness between two pixels) is

$$I_{p,q} = 1 - \frac{\parallel \mathbf{s}(\mathbf{x}_p) - \mathbf{s}(\mathbf{x}_q) \parallel}{max\{\parallel \mathbf{s}(\mathbf{x}_{\cdot}) \parallel\} - min\{\parallel \mathbf{s}(\mathbf{x}_{\cdot}) \parallel\}} \quad \mathbf{x}_p, \mathbf{x}_q \in \mathbb{N}^d, \mathbf{s}_p, \mathbf{s}_q \in \mathbb{R}^m$$
(9)

Spatial closeness $\mathcal{D}_{p,q}$ (i.e., the spatial correlation between two pixels) is

$$D_{p,q} = \frac{\phi(\parallel \mathbf{x}_p - \mathbf{x}_q \parallel)}{\phi(\parallel 0 \parallel)} \quad \mathbf{x}_p, \mathbf{x}_q \in \mathbb{N}^d$$
 (10)

where $\phi(\cdot)$ denotes the Gaussian function. As shown in Fig. 5, if two pixels are far away from each other, the spatial correlation between them is low. In other words, $\phi(\parallel \mathbf{x}_p - \mathbf{x}_q \parallel) < \phi(\parallel \mathbf{x}_p - \mathbf{x}_{q'} \parallel)$ while $D_{p,q} > D_{p,q'}$.

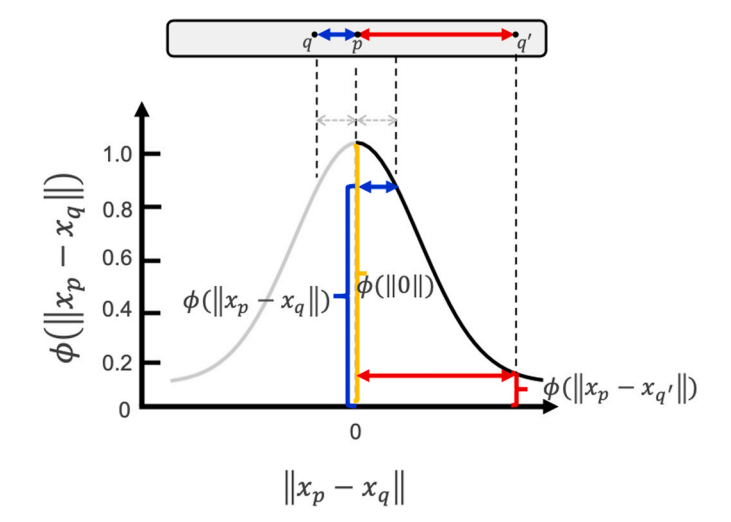


Fig. 5. The relationship of $\phi(\parallel \mathbf{x}_p - \mathbf{x}_q \parallel)$ and spatial distance. If two pixels are far away from each other, the spatial correlation between them is tend to be low. In other words, $\phi(\parallel \mathbf{x}_p - \mathbf{x}_q \parallel) < \phi(\parallel \mathbf{x}_p - \mathbf{x}_q \parallel)$ while $D_{p,q} > D_{p,q}$.

The adjacency matrix $\mathbf{A}_{p,q}$ is derived as a binary matrix where $\mathbf{A}_{p,q}=1$ if there is a link from node p to node q, and otherwise if they are not connected:

$$\mathbf{A}(\mathbf{x}_{p}, \mathbf{x}_{q}) = \Theta(\varepsilon - w_{p,q}) - \Delta_{p,q} \tag{11}$$

where ε denotes the threshold, Θ is the Heaviside Function, and $\Delta_{p,q}$ is the Kronecker delta which prevents the self-loop in the recurrence network. The threshold ε is often chosen based on the significance level α . Note that the 0.05 significance level is the most commonly used α value in statistics. In this study, we set $\alpha=0.05$.

3.4. Network characterization and quantification

Network statistics are established measurements for the characterization of the topology, and provide useful information for statistical

Table 2Network measures and the corresponding mathematical expressions.

Quantifiers	Expression	Description
Degree	$k_p = \Sigma_{q=1}^N A_{p,q}$	Number of edges connected to node <i>p</i> . <i>N</i> denotes the number of node in the network.
Betweenness centrality	$BC_p = \sum_{p eq q eq r} rac{\sigma_{qr} p}{\sigma_{qr}}$	σ_{qr} is the total number of paths from node q to node r , $\sigma_{qr}p$ is the number of those paths which pass through node p .
Pagerank centrality	$PR_p = (1 - \alpha)\frac{1}{N} +$	$\alpha \in (0, 1), L_q$ is the number of neighbors of node q .
	$\alpha \sum_{q} A_{qp} \frac{PR_q}{L_q}$	
Closeness centrality	$egin{aligned} lpha \sum_q & rac{PR_q}{L_q} \ & C_p = rac{1}{\Sigma_{p eq q} d_{p,q}} \ & V_p = rac{1}{\lambda} \Sigma_{q \in M(q)} V_q \end{aligned}$	$d_{p,q}$ is the distance between node p and node q .
Eigenvector centrality	$V_p = rac{1}{\lambda} \Sigma_{q \in M(q)} V_q$	$M(q)$ denotes the set of neighbors of p , λ is a constant.

inference as well as predictive modeling [28]. Table 2 summarizes the network statistics and their corresponding mathematical equations used in this study.

In the proposed GRN framework, degree k_p represents the recurrence frequency relative to the pixel p. In other words, the distribution of k_p shows the recurrence distribution of spatial data. The centrality measurements reveal recurrence patterns between a node and its neighbors. For example, the betweenness centrality quantifies the number of shortest paths that pass through one node, which indicates how many times a node appears in different patterns. Eigenvector centrality is a measure of the influence of a node in a network, and pagerank centrality is its variant. The bigger the eigenvector centrality, the more a node impacts other nodes in a network. The closeness centrality is calculated as the reciprocal of the sum of the shortest paths between the node and all other nodes in the network. The node with larger closeness centrality is closer to other nodes, and indicates a stronger recurrence pattern.

3.5. Hypothesis testing

We tested the statistical significance of extracted network features using the Mann-Whitney U test [29]. Let X and Y denote two histograms, and contain m and n observations, respectively. The hypothesis of the Mann-Whitney U test is

$$H_0$$
: Two histograms *X* and *Y* follow the same distribution H_1 : Two histograms *X* and *Y* follow different distributions (12)

Mann-Whitney U test begins by arranging the m+n observations in a single sequence from the smallest to the largest. Then, a rank is assigned to each element corresponding to the position. That is, each of the observation is assigned a rank from 1 to m+n in the ordering. If H_0 is true, the observations X_1, \ldots, X_m (or Y_1, \ldots, Y_n) tend to be dispersed throughout the ordering of all m+n observations. Otherwise, the observations are concentrated among the smaller values or among the larger values if H_1 is true. Let S denote the sum of the ranks assigned to m observations from X. Given H_0 is true,

$$E(S) = \frac{m(m+n+1)}{2}$$
 (13)

and

$$Var(S) = \frac{mn(m+n+1)}{12}.$$
 (14)

Note that when the H_0 is true and sample size m and n are large, the distribution of S is approximately normal. The null hypothesis H_0 is rejected if $|S-(1/2)m(m+n+1)| \geq c$, where $c=[Var(S)]^{1/2}\Phi^{-1}(1-\alpha/2)$. The p-value is computed as $2[1-\Phi(z_0)]$ where $z_0=|S-E(S)|/\sqrt{Var(S)}$. If the p-value is less than the significant level (i.e., $\alpha=0.05$), H_0 will be rejected and the distributions of X and Y are

declared to be different at the significance level of 0.05.

3.6. ANOVA and predictive modeling

Further, we perform an ANOVA to study the effects of experimental factors (i.e., orientations and other design parameters) on the build quality. Here, the parameters of contour space, thin-wall width, and height are associated with the thin-wall number. In total, there are three levels for orientation O and 21 levels for thin-wall characteristics $\mathscr C$. The last four thin-walls collapsed during the fabrication process (see Fig. 1). Therefore, we only take the other 21 thin-walls into account in the ANOVA. We reorganize our design parameters into two groups, i.e., orientation and thin-wall characteristics, with 3 levels and 21 levels, respectively.

Two-way ANOVA is commonly performed when there are two factors (i.e., factor M with m levels and factor N with n levels) in an experiment. Fig. 6 shows the data structure for ANOVA, which is expressed as:

$$X_{ij} = \mu + O_i + \mathscr{C}_j + O\mathscr{C}_{ij} + \epsilon_{ij}$$
(15)

where $i=1,\ldots,3, j=1,\ldots 21$, and ϵ_{ij} represents the error term in the model.

In addition, we develop a regression model to predict the effects of design parameters on network characteristics.

$$y = \beta_0 + \beta_1 \times O_1 + \beta_2 \times O_2 + \beta_3 \times W + \beta_4 \times H + \beta_5 \times G + \beta_6 \times O_1 \times W + \beta_7 \times O_2 \times W + \beta_8 * O_1 \times H + \beta_9 \times O_2 \times H + \beta_{10} \times O_1 \times G + \beta_{11} \times O_2 \times G + \beta_{12} \times W \times H + \beta_{13} \times W \times G + \beta_{14} \times H \times G + \varepsilon$$

$$(16)$$

where the categorical variable O is coded with O_1 and O_2 , and stands for the orientation (see Table 3). W denotes the width, H represents the height of a thin-wall, and G indicates the contour space. Note that in Eq. (16), the explanatory variables are the design parameters and the response variable y is the Hotelling's T^2 statistic that is computed for the i^{th} observation as $T^2(i) = (\mathbf{x}^{(i)} - \overline{\mathbf{x}})^T \mathbf{S}^{-1} (\mathbf{x}^{(i)} - \overline{\mathbf{x}})$, where $\mathbf{x}^{(i)}$ is the vector of network features, $\overline{\mathbf{x}}$ is the mean vector and S is the covariance matrix.

4. Experimental results

The proposed methodology is evaluated and validated with both simulation and real-world case studies. First, we derive the visualization results of GRN and extract corresponding network from simulated images with different types of defects (i.e., edge variations and surface characteristics). Then, we perform pair-wise hypothesis tests on the extracted quantifiers. The simulation study is aimed at testing the significance of quantifiers with defect variations. Next, in the real-world case study, we leverage the proposed GRN to characterize the quality of PBF-AM builds and study the relationships between the design parameters (i.e., build orientation, contour space, thin-wall height, and width) and quality characteristics of thin-wall structures. Finally, we develop a regression model to predict how the design complexity impacts the GRN behaviors in each layer of thin-wall builds.

4.1. Simulation study

As shown in Table 4, two types of defect patterns (i.e., edge variation and inner surface variation) are simulated to evaluate the visualization and the performance of the proposed GRN methodology. The size and location of porosity defects are varied to simulate three different levels of inner surface variations.

Fig. 7 shows the heatmap of the real XCT scan (top) and the simulated XCT scan (bottom). Note that the real-world XCT scan is taken from the layer 100 of thin-wall 13 in the part built under orientation 60°. It may be noted that the thin-wall has both edge variation and inner surface issues (i.e., porosity). Therefore, we add variations to edges and



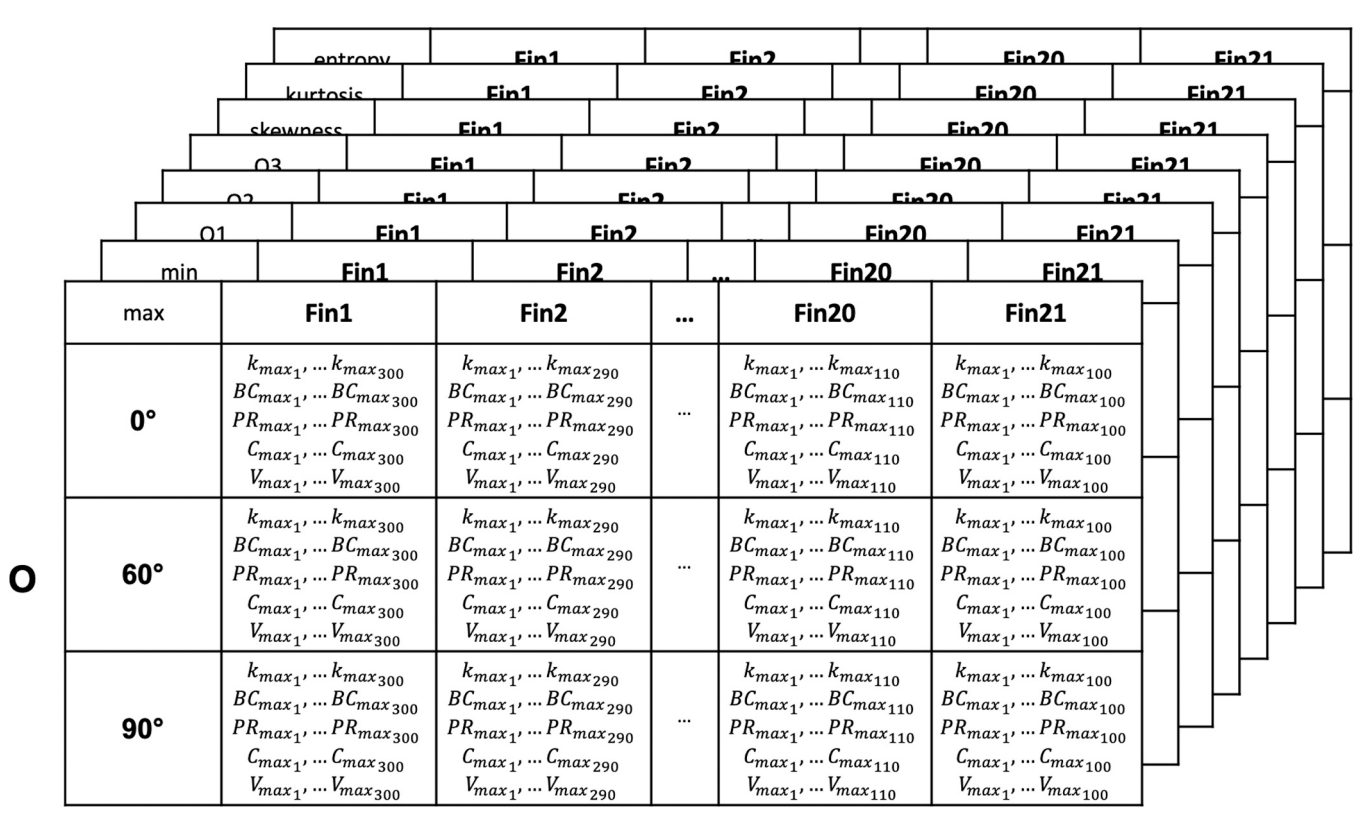


Fig. 6. Experimental data structure for the ANOVA analysis: @ and O represent two factors, namely thin-wall characteristics and orientation.

Table 3Coding for the categorical variable orientation.

	O_1	O_2
Orientation 0°	0	0
Orientation 60°	1	0
Orientation 90°	0	1

Table 4Defect variation in the simulation study.

Category	Case	Description		
	Baseline	A thin-wall without any flaws		
Edge variation	Case I	Edge roughness with the frequency of 100 Hz		
	Case II	Edge roughness with the frequency of 200 Hz		
	Case III	Edge roughness with the frequency of 400 Hz		
Number of pores variation	Case IV	Three pores each with a diameter of 4 pixels		
	Case V	Six pores each with a diameter of 4 pixels		
	Case VI	Nine pores each with a diameter of 4 pixels		
Size of pores variation	Case VII	Six pores each with a diameter of 2 pixels		
	Case VIII	Six pores each with a diameter of 4 pixels		
	Case IX	Six pores each with a diameter of 6 pixels		

surfaces in the baseline to generate different types of defects, see Table 4. In addition, it can be seen that the real XCT scan (see Fig. 7 (a)) shows a transition of pixel values on the edge, i.e., from the yellow region to the blue region. We have also added this transition to the simulated XCT.

Fig. 8 shows the network visualization and the distribution of



Fig. 7. Proportional heatmap of the XCT scan from thin-wall 13, layer 100 in the thin-wall part built under orientation 60°, and proportional heatmap of the simulated baseline thin-wall. Note that the blue color represents nodes with smaller pixel values, and the yellow color is corresponding to bigger values in the gray scale. (For interpretation of the references to color in this figure legend, the reader is referred to the web version of this article.)

network quantifiers (i.e., degree k, betweenness centrality BC, pagerank centrality PR, closeness centrality C, and eigenvector centrality V) for the baseline case (Simulated XCT in Fig. 7). Note that nodes in the network are clustered into two groups. In the network, yellow nodes (i. e., laser-fused area) are clustered into one group and blue nodes (i.e., powder area) are clustered into another group, and two groups are connected. Peaks shown in Fig. 8 (b) are corresponding to the degree distribution in two clusters. For example, the smaller peak is related to the cluster of laser-fused surface (i.e., yellow nodes) with less number of nodes in the network, and the bigger peak is relevant to the powder area cluster (i.e., blue nodes). The baseline distributions of network features (Fig. 8 (b)–(f)) will be benchmarked with the following simulation scenarios.

First, we explore the relationship between edge variation and network characteristics, as shown in Fig. 9. In case I, we utilize a sine wave with an amplitude of 15 and a frequency of 100 Hz to generate the edge variation. Then, we increase the frequency to 200 and 400 Hz for case II and case III, respectively.

As shown in Fig. 10, nodes in background and surface are clustered into three different groups in all networks. The blue cluster represents

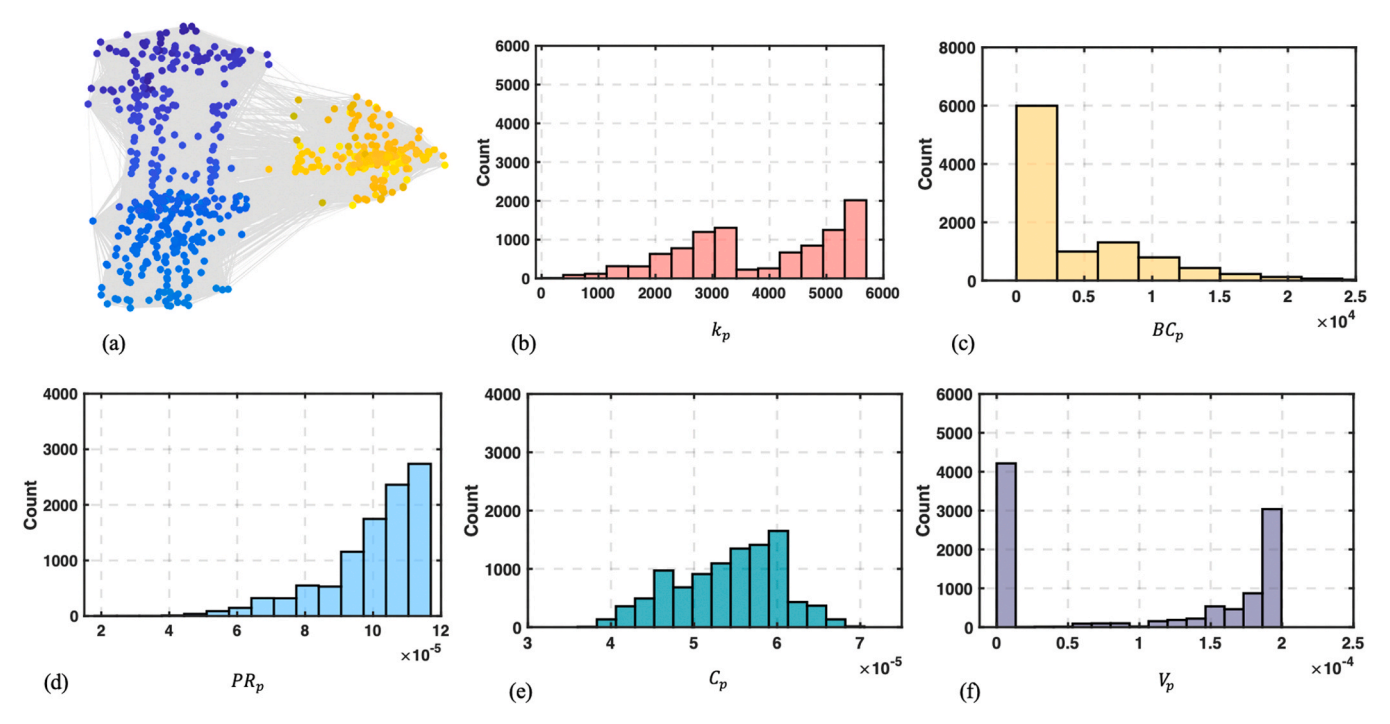


Fig. 8. (a) Network visualization of the simulated baseline thin-wall in Fig. 7. (b)–(f) Distributions of *k*, *BC*, *PR*, *C*, and *V*. (For interpretation of the references to color in this figure legend, the reader is referred to the web version of this article.)

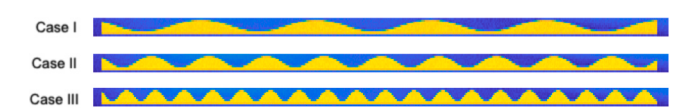


Fig. 9. Simulated thin-walls with edge variation of different frequencies. Case I: 100 Hz, case II: 200 Hz, case III: 400 Hz.

the powder area, the yellow nodes correspond to the laser-fused layerwise surface, and the green nodes are related to the transitions on the edges, which appear as a "bridge" linking the blue cluster and the yellow cluster. Fig. 10 (b) and (c) shows more variations on the edge (i.e., the frequencies are higher) compared to Fig. 10 (a). Therefore, the green cluster becomes more dispersed as the variation increases. Distributions of network quantifiers for the case I-III are shown in Fig. 11. Each degree distribution contains two peaks corresponding to the blue and yellow clusters. In comparison with the baseline case which also has two peaks (see Fig. 8 (b)), the number of nodes with lower degrees (i.e., 1–500) increases and the number of nodes with the degree around 2000-3000 decreases significantly. The peak between 0 and 500 is from the edge cluster and is not as high as the others because the edge contains a smaller number of nodes. Also, the number of nodes with a degree around 4500 significantly increases as the edge variation increases. In addition, the increment of edge variation is positively correlated with the number of nodes with closeness centrality of 5.25e-5, and is

negatively related to the number of nodes with closeness centrality of 6.25e-5. In summary, the distributions of network quantifiers vary between cases I–III and the baseline.

We perform the Mann-Whitney U test for pairwise comparison between histograms among different simulation cases. The statistically significant results are marked bold in Table 5. Note that, case I and case II, and case I and case III are significantly different for five quantifiers, but the GRN quantifiers of case II and case III only differ in degree and eigenvector centrality according to the p-values in Table 5.

Next, we add porosity defects to the simulated thin-wall (i.e., the baseline case). Each pore has the diameter of 4. Three pores are firstly included to the laser-fused surface area (case IV). Then, we increase the number of pores to six in case V, and nine pores in case VI as shown in Fig. 12. Similarly, three clusters corresponding to the edge, laser-fused area, and the powder area can be seen among all the networks in Fig. 13. However, the edge cluster (in green) does not contain as many nodes as in Fig. 10. This is because (1) there is no edge variations in these cases, and (2) the number of transitional pixels on the edge is limited. Note that the number of nodes in the circled cluster increases as the number of pores increases in (a) and (b). It is challenging to visually find individual groups representing different pores among networks. Here, we keep all parameters the same for further quantification analysis in our simulation study. In Fig. 14, the first row (i.e., in red) show the distribution of k and the peak around 5000 drops while more pores are

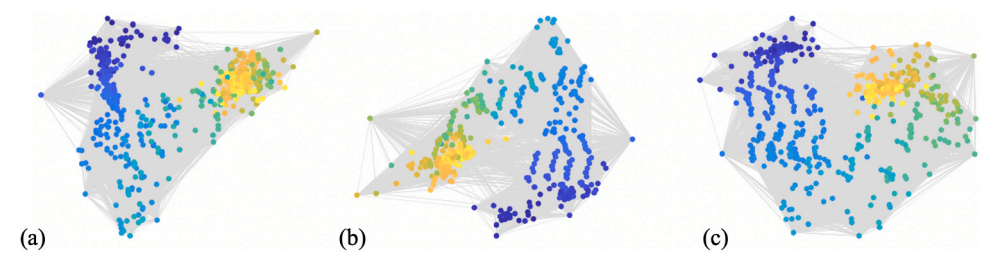


Fig. 10. Network visualization results of the GRNs in Fig. 9. (a) case I, (b) case II, and (c) case III. (For interpretation of the references to color in this figure legend, the reader is referred to the web version of this article.)

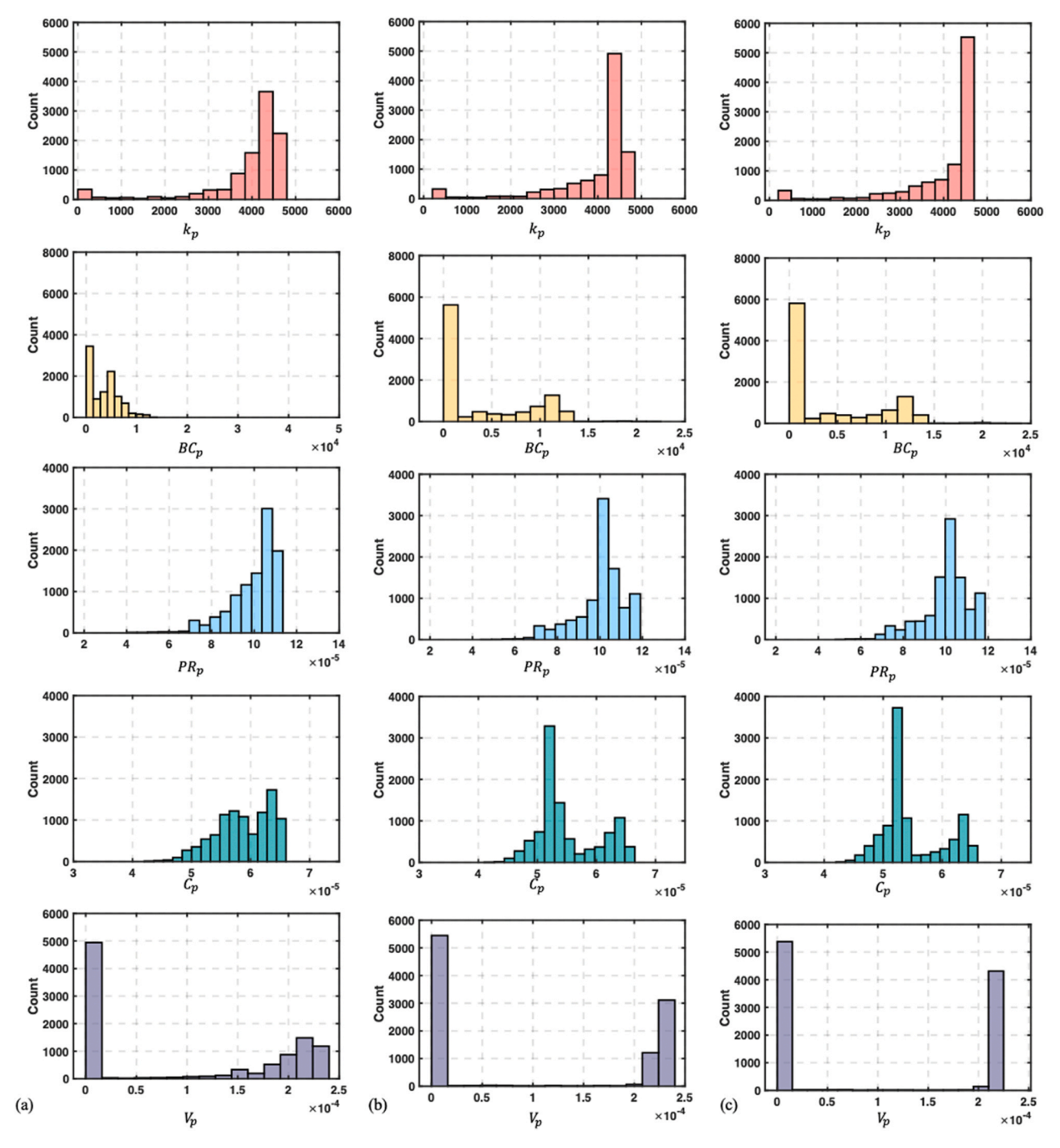


Fig. 11. The distribution of k, BC, PR, C, and V in GRNs for 3 cases in Fig. 9. (a) case I, (b) case II, and (c) case III.

Table 5Two-sample Mann-Whitney U testing of quantifier distributions among simulation cases I–III.

	Case I vs. Case II	Case I vs. Case III	Case II vs. Case III
k	1.124e-5	5.368e-22	2.495e-24
BC	2.447e-17	5.501e-28	0.395
PR	3.488e-08	1.809e-09	0.777
C	0	0	0.2923
V	8.445e-17	2.252e-140	0

Bold values mark statistically significant results where p-values of Mann-Whitney U tests are less than 0.05 (i.e., alpha).



Fig. 12. Simulated thin-walls with pores of same size (diameter 4 pixels) but different number of pores. Case IV: 3 pores, case V: 6 pores, case VI: 9 pores.

added to the laser-fused area. Similarly, the peak of *PR* at the x-axis with the value of 10e-5 decreases when the number of pores increases. However, as shown in Table 6, the hypothesis test does not indicate there exist significant variations in pagerank centrality among pairwise comparisons. The variation is not enough to suggest any differences at

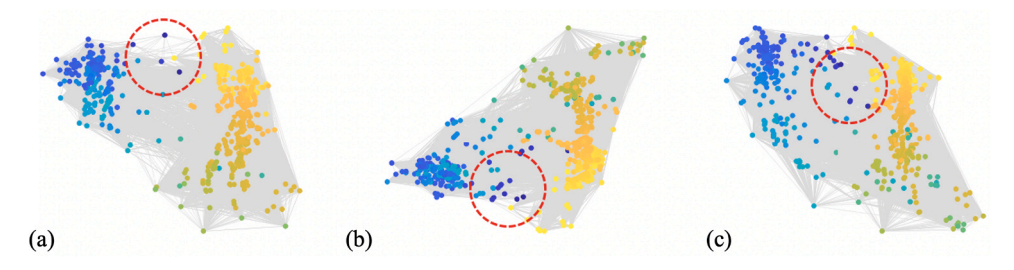


Fig. 13. Network visualization results of the GRNs in Fig. 12. (a) case IV, (b) case V, and (c) case VI.

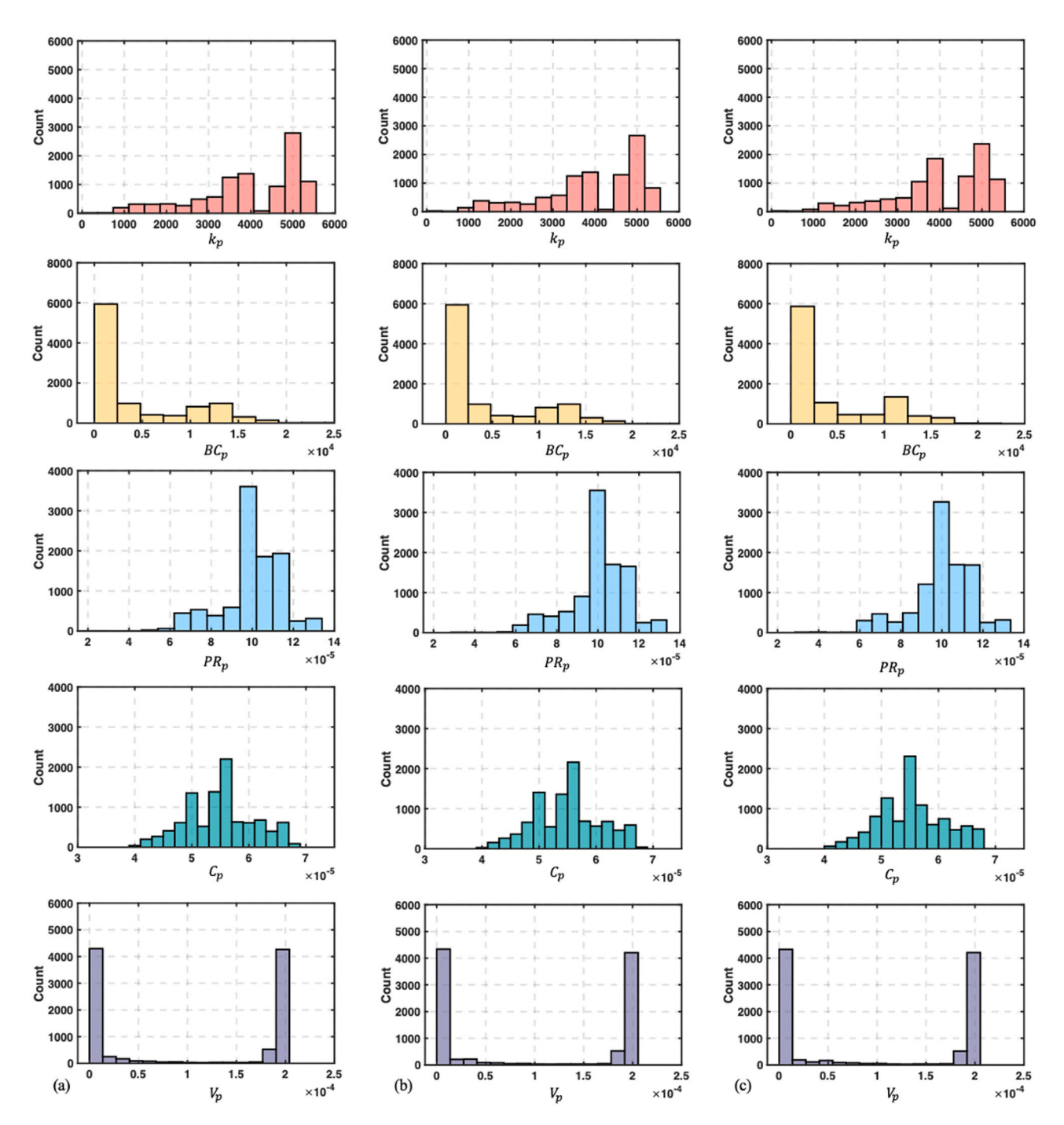


Fig. 14. The distribution of *k*, *BC*, *PR*, *C*, and *V* in GRNs for 3 cases in Fig. 13. (a) case IV, (b) case V, and (c) case VI. (For interpretation of the references to color in this figure legend, the reader is referred to the web version of this article.)

Table 6
Two-sample Mann-Whitney U testing of quantifier distributions among simulation cases IV–VI.

	Case IV vs. Case V	Case IV vs. Case VI	Case V vs. Case VI
K	2.664e-04	0.497	3.941e-5
BC	0.022	0.442	0.303
PR	0.839	0.895	0.895
C	0.282	3.105e-5	5.03e-9
V	2.738e-18	1.984e-20	0.0246

Bold values mark statistically significant results where p-values of Mann-Whitney U tests are less than 0.05 (i.e., alpha).

the significance level of 0.05. Also, it can be seen from the results that the eigenvector centrality is sensitive to the number of pores in the fin part since the p-values are less than 0.05.

Finally, three more cases are designed with the pore diameters selected as 2, 4, and 6 respectively as shown in Fig. 15. Fig. 16 shows that the cluster associated with porosity defect is more noticeable when the size of the pore becomes bigger (see red circles). The number of nodes in the cluster increases as the size of pore increases. Fig. 17 shows the distributions of their quantifiers, and Table 7 presents the result of pair-wise hypothesis tests. Degree k, betweenness centrality (BC), closeness centrality (BC), and eigenvector (BC) contrality track the changes in the size of porosity. Note that pagerank centrality (BC) does not vary significantly in both Table 6 and Table 7, and is not sensitive to the porosity defect on the surface of thin-wall.

The proposed GRN method provides a complete picture of spatial patterns and recurrence behaviors through the network visualization and hypothesis testing. Network structures have different patterns with respect to simulated thin-wall images in cases I–IX. From the simulation study, we select the set of five quantifiers (i.e., degree k, betweenness centrality BC, pagerank centrality PR, closeness centrality C, and eigenvector centrality V) that are sensitive to both powder area and laser-fused area in various cases. Note that distributions of quantifiers show different shapes regarding different quality issues. For example, when edge variation increases, there is an increase in the peak among distributions in Fig. 11. Also, the p-values two sample Mann-Whitney U test indicates the differences between distributions of quantifiers. In the real-world case study, we extract features (i.e., maximum, minimum, quartiles, standard deviation, skewness, kurtosis, and entropy) from these selected quantifiers for further analysis.

4.2. Real-world case study

We extracted 9 features from each distribution of network quantifiers, i.e., the maximum value, the minimum value, the standard deviation, quartiles (Q1, Q2, Q3), skewness, kurtosis, and entropy. In total, 45 features from 5 quantifiers of each network are extracted where one thin-wall of one layer generates a recurrence network. Fig. 18 shows distributions of Q1s of degree (k), betweenness centrality (BC), and pagerank centrality (PR), respectively. Note that the distributions are approximately normal. As shown in Fig. 18 (a), the Q1 of degree does not vary significantly between parts built under three orientations. However, they are vastly different for the betweenness centrality (Fig. 18 (b)) and the pagerank centrality (Fig. 18 (c)).

We perform two-way ANOVA on total of 45 features, and then calculate the Hotelling's T^2 statistic for each thin-wall based on the first seven components (i.e., according to the Kaiser rule) to quantify the

relationship between design complexity and the network features (Table 8).

The regression model yields the R-squared statistic of 87.12% and the adjusted R-squared statistic of 87.08%, which demonstrates that the variations in response variable (i.e., the Hotelling's T^2 statistic) are highly correlated with the design parameters. Note that the R-squared statistic is defined as $R^2 = 1 - \frac{\text{Sum of Square}_{\text{residual}}}{\text{Sum of Square}_{\text{total}}} = 1 - \frac{\Sigma_i(T(i) - \hat{T}(i))}{\Sigma_i(T(i) - \hat{T})}$, where T (i) is the Hotelling's T^2 statistic, $\hat{T}(i)$ is the predicted value, and T is the overall average. The normal Q-Q plot (Fig. 19) illustrates that the normality assumption is valid because the plot approximately follows a straight line.

In our experiment, quality is inversely proportional to the amount of defects (e.g., lack of fusion, inconsistency, porosity, and edge variation). However, summary statistics tend to be limited in the ability to characterize and quantify complex defect patterns in layerwise images. Therefore, we propose the generalized recurrence network method to effectively represent the spatial imaging data, then leverage network visualization and quantifiers to capture various forms of defect patterns. Experimental results from hypothesis testing showed these network quantifiers are effective and sensitive to different defect patterns. These network quantifiers are then used to interpret and describe the level of quality for each layer of the build, which are further utilized to establish predicative models to investigate how design parameters (e.g., build orientation, thin-wall width, thin-wall height, and contour space) impact the quality characteristics in thin-wall builds. In addition, experimental results show that four thin-walls (width $\leq 0.1 \text{ mm}$) collapsed regardless of what orientation is utilized in the fabrication process. Therefore, only thin-walls with the width greater than 0.1 mm can be printed by the PBF machine are utilized in this study. Thin-walls with the width greater than 0.1 mm printed under orientation 0° generate results with better quality. The result also shows that the quality decreases when the layer number goes up, which may cause by the defect propagation when printing the build layer by layer or by the different thermal conditions between the bottom and the top of each thin wall. We also found that the layer quality varies less in thin-wall builds with orientation 0° in comparison with orientation 60° and orientation 90°. Also, the thin-wall build with orientation 60° is more sensitive to the changes in contour space compare to the other two orientations. Therefore, the orientation 60° should be avoided while printing thin-wall structures. Although in our experiment, thin-walls 1-24 and the thin-wall 25 have built with two different hatching patterns, contour space within the thin-wall decreases from thin-wall 1 to thin-wall 25. Also, the collapse occurs in both types of hatching patterns. Hatching patterns of the thin-wall are not controllable factors in this

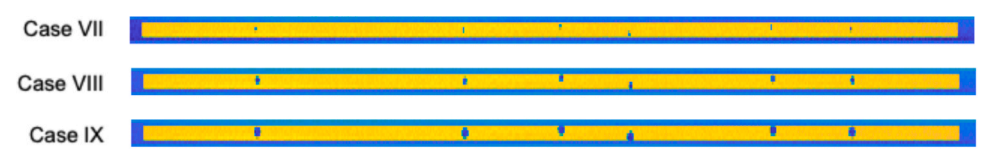


Fig. 15. Simulated thin-walls with different pore sizes but same number of pores. Case VII: diameter 2 pixels, case VIII: diameter 4 pixels, case VII: diameter 6 pixels.

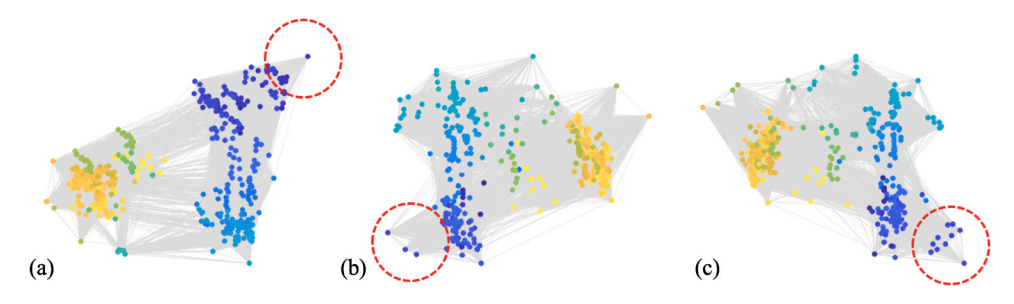


Fig. 16. Network visualization results of the GRNs in Fig. 15. (a) case VII, (b) case VIII, and (c) case IX. (For interpretation of the references to color in this figure legend, the reader is referred to the web version of this article.)

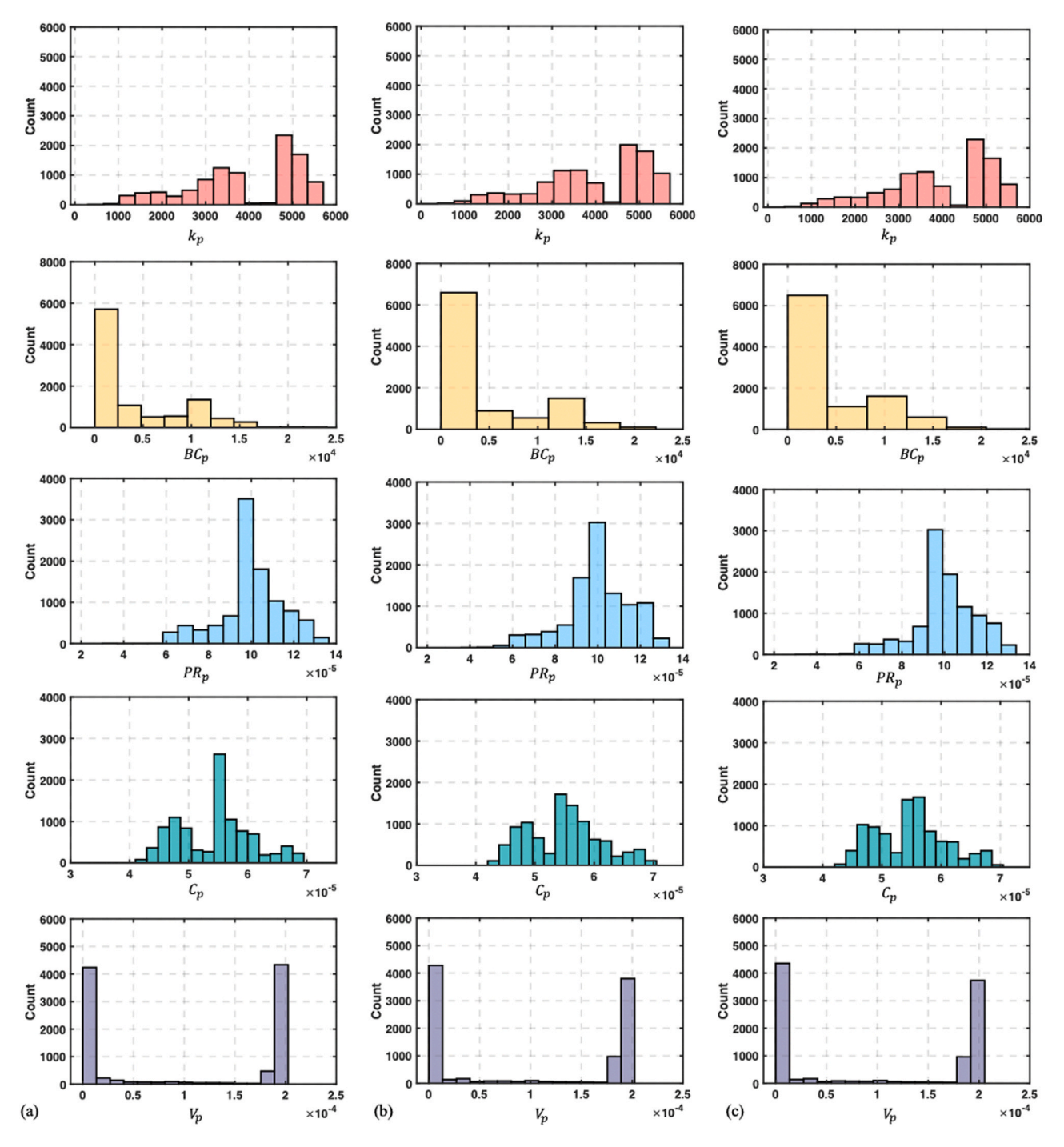


Fig. 17. The distribution of k, BC, PR, C, and V in GRNs for 3 cases in Fig. 16. (a) case VII, (b) case VIII, and (c) case IX.

Table 7Two-sample Mann-Whitney U testing of quantifier distributions among simulation cases VII–IX.

	Case VII vs. Case VIII	Case VII vs. Case IX	Case VIII vs. Case IX
k	0.035	4.739e-4	1.394e-8
BC	0.474	0.004	0.083
PR	0.965	0.340	0.340
C	1.804e-8	1.787e-4	0.089
V	1.234e-6	4.078e-47	1.998e-27

Bold values mark statistically significant results where p-values of Mann-Whitney U tests are less than 0.05 (i.e., alpha).

study because of the automatic settings by the EOS M280 PBF machine.

5. Discussions and conclusions

PBF-AM provides the design freedom that cannot be realized by traditional manufacturing techniques such as cutting, milling and casting. PBF-AM provides the design freedom that cannot be realized by traditional manufacturing techniques such as cutting, milling and casting. Engineers may come up with different designs. These designs may have different levels of complexity. A higher level of design complexity tends to degrade the quality of final PBF-AM builds and lower the repeatability of the process. Realizing high quality and repeatability call upon the development of sensor-based monitoring and control of PBF processes. Advanced imaging leads to a rich data environment for AM quality control. However, the structure of spatial data is often high-dimensional with complex geometric patterns. Therefore, there is an urgent need to extract quality characteristics from spatial imaging data and further explore the design-quality relationship for engineering designs.

Machine learning methods are commonly used in the AM community to process image profiles and build predictive models that require minimal feature engineering [30]. For example, contemporary machine algorithms can help to optimize process parameters, and conduct examination of powder spreading and in-process defect monitoring. Recently, there have been increasing interests in using deep learning models for prediction in AM. For example, Zhang et al. [31] investigated the relationship between the mechanisms underlying the layer-by-layer printing process and the resulting product quality through an LSTM network, Mozaffar et al. [32] proposed a recurrent neural network for predicting the high-dimensional thermal history in the AM process. Francis et al. [33] developed a novel Deep Learning approach that accurately predicts distortion within LBAM tolerance limits by considering the local heat transfer. Although deep learning yielded a high predictive power in many studies, they need large amounts of data to study patterns hidden in the AM signals. Also, drawbacks of these deep learning models include high computational cost and black-box approaches lacking physical interpretations.

In this paper, we propose a generalized recurrence network method to visualize the complex spatial patterns in additive manufacturing

Table 8 Example of two-way ANOVA for assessing the significance of $\mathscr C$ and O on max (k).

Source	Sum Sq.	d.f.	Mean Sq.	F	Prob > F
C	2.686e9	20	1.343e8	676.184	0
O € *0	2.621e7 3.010e7	2 40	1.311e7 7.525e5	65.985 3.788	3.112e-29 9.058e-15
Error Total	2.491e9 5.235e9	12,537 12,599	1.987e5	5.760	3.000c-13

Bold values mark statistically significant results where p-values of ANOVA are less than 0.05 (i.e., alpha).

Table 9Results of regression analysis.

Effect	Variable	Estimate	Error	t value	p-value
β_0	-	2.242	0.331	6.782	1.323e-11
β_1	O_1	2.449	0.294	8.302	1.307e-16
β_2	O_2	1.444	0.295	4.891	1.034e-6
β_3	W	34.885	5.419	6.438	1.327e-10
β_4	H	-0.962	0.310	-3.108	1.985e-3
β_5	G	-104.504	5.173	-20.201	2.699e-87
β_6	$O_1 imes W$	-45.105	5.158	-8.745	3.001e-18
β_7	$O_2 \times W$	-24.270	5.160	-4.704	2.621e-6
β_9	$O_2 \times H$	-0.318	0.039	-8.260	1.853e-16
β_{10}	$O_1 imes G$	50.139	5.241	9.567	1.683e-21
β_{11}	$O_2 imes G$	27.216	5.242	5.192	2.165e-7
β_{13}	$W \times G$	269.259	3.623	74.311	0

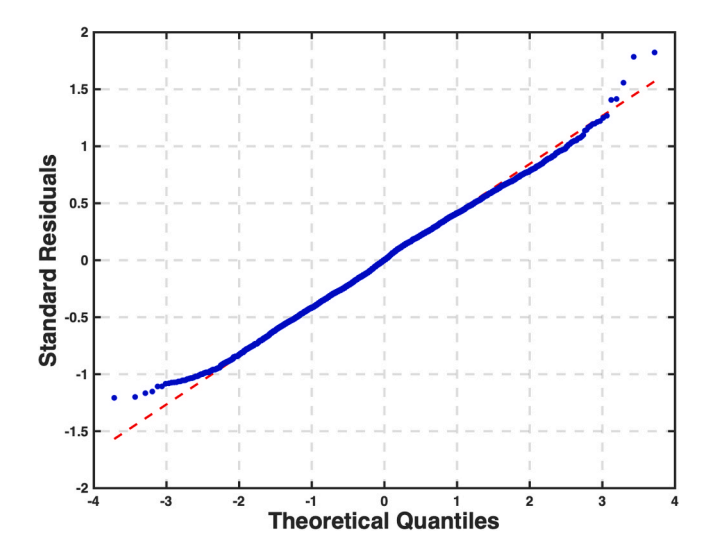
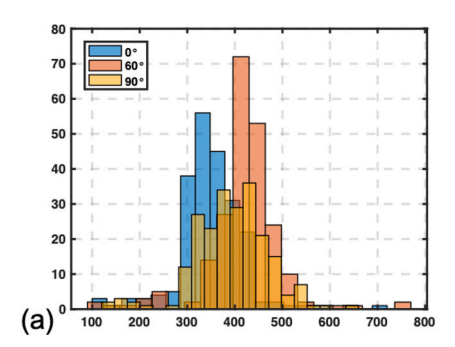
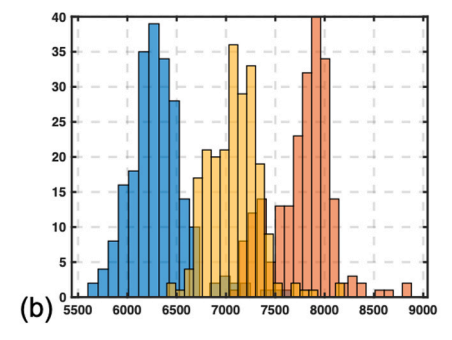


Fig. 19. Normal Q-Q plot of the regression model.





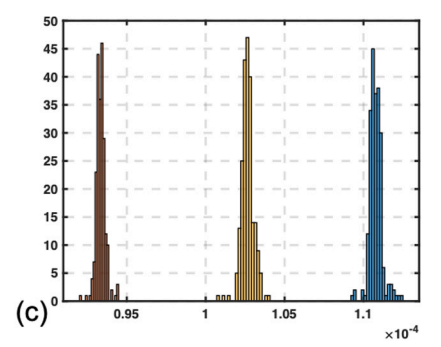


Fig. 18. The distribution of (a) Q1 (k); (b) Q1 (BC); (c) Q1 (PR) of thin-wall 8 over all layers.

images, and introduce network quantifiers to characterize recurrence properties across layers. The proposed GRN method can not only extend to high-dimensional data, but also effectively capture the complex defect patterns in spatial imaging data. We leverage high-resolution post-build XCT scan data to analyze the relationship between design parameters and PBF-AM builds through a GRN framework. First, we generate layerwise images from 3D XCT data and register these images to the CAD model layer by layer. Then, the proposed GRN is utilized to extract the quality-related quantifiers from registered images. Next, we perform a design of experiment to investigate the relationship between design parameters and network quantifiers in thin-wall builds. Finally, a regression model is developed to predict the behavior of network features from the design parameters. Experimental results demonstrate that thin-wall build quality is sensitive to build orientation, thin-wall height, thin-wall width, and contour space. Thin-walls with the width bigger than 0.1 mm printed under orientation 0° are found to yield better quality compared to 60° and 90°, and the thin-wall build with orientation 60° is more sensitive to the changes in contour spacee compare to the other two orientations.

Network models are flexible and generally applicable to different data forms (e.g., time series [34,35], two-dimensional image data [36, 27,37], three-dimensional voxel data [38]). AM provides a higher level of flexibility for the low-volume and high-mix production, even for a one-of-a-kind design. AM fabricates the build directly from a complex CAD design through layer-upon-layer deposition of materials. Each image contains not only metal powders but also many AM parts in the build plate. As such, there is a need to delineate the image for a specific part. In this paper, we register the ROI to the part geometry in each layer, i.e., a rectangle region in each layer of the thin-wall build. However, ROI registration is generalizable to different part geometries, even complex designs with layerwise variations as long as the CAD design files are readily available, as shown in Fig. 4. The presented study sheds insights into the optimization of engineering design for quality improvements of PBF-AM builds. Future works may focus on the optimization of design parameters, hatching patterns and process settings to improve the quality of thin walls.

CRediT authorship contribution statement

Ruimin Chen: Conceptualization, Methodology, Software, Data curation, Writing - original draft. Prahalad Rao: Conceptualization, Methodology, Data curation, Writing - review & editing, Resources. Yan Lu: Supervision, Conceptualization, Writing - review & editing, Resources. Edward W. Reutzel: Conceptualization, Writing - review & editing, Validation. Hui Yang: Supervision, Conceptualization, Methodology, Writing - original draft, Writing - review & editing, Funding acquisition.

Declaration of Competing Interest

The authors declare that they have no known competing financial interests or personal relationships that could have appeared to influence the work reported in this paper.

Acknowledgement

The authors (RC, ER, and HY) would like to thank National Institute of Standards and Technology (NIST) for the support of this research work. We gratefully acknowledge the valuable contributions of the CIMP-3D at Penn State providing the data utilized in this research, in particular Corey Dickman for designing and executing the test builds, Griffin Jones for performing the CT scans, and students Gabi Gundermann and Matt Dolack for preliminary analysis. The author (PR) thanks the National Science Foundation (NSF) for funding his work under awards OIA-1929172, CMMI-1719388, CMMI-1920245, CMMI-1739696, and CMMI-1752069. Understanding the causal influence of

process parameters on part quality and defect formation via data-driven modeling was the major aspect of CMMI-1752069 (Program Officer: Kevin Chou). Supplemental funding for CMMI-1752069 was obtained through the NSF INTERN program (Program Officer: Prakash Balan) and CMMI Data Science Activities (Program Officer: Martha Dodson) is greatly appreciated.

Disclaimer

Certain commercial equipment, or materials, suppliers, or software are identified in this paper to foster understanding. Such identification does not imply recommendation or endorsement by the National Institute of Standards and Technology, nor does it imply that the materials or equipment identified are necessarily the best available for the purpose.

References

- B.P. Conner, G.P. Manogharan, A.N. Martof, L.M. Rodomsky, C.M. Rodomsky, D. C. Jordan, J.W. Limperos, Making sense of 3-d printing: creating a map of additive manufacturing products and services, Addit. Manuf. 1 (2014) 64–76.
- [2] J. Liu, C. Liu, Y. Bai, P. Rao, C.B. Williams, Z. Kong, Layer-wise spatial modeling of porosity in additive manufacturing, IISE Trans. 51 (2) (2019) 109–123.
- [3] S.H. Huang, P. Liu, A. Mokasdar, L. Hou, Additive manufacturing and its societal impact: a literature review, Int. J. Adv. Manuf. Technol. 67 (5–8) (2013) 1191–1203.
- [4] B. Lyons, Additive manufacturing in aerospace: examples and research outlook, Bridge 44 (3) (2014) 13–19.
- [5] Y. Jin, S.J. Qin, Q. Huang, Modeling inter-layer interactions for out-of-plane shape deviation reduction in additive manufacturing, IISE Trans. 52 (7) (2020) 721–731.
- [6] K. Bastani, P.K. Rao, Z. Kong, An online sparse estimation-based classification approach for real-time monitoring in advanced manufacturing processes from heterogeneous sensor data, IIE Trans. 48 (7) (2016) 579–598.
- [7] N. Marwan, J. Kurths, P. Saparin, Generalised recurrence plot analysis for spatial data, Phys. Lett. A 360 (4–5) (2007) 545–551.
- [8] F. Imani, A. Gaikwad, M. Montazeri, P. Rao, H. Yang, E. Reutzel, Layerwise in-process quality monitoring in laser powder bed fusion, in: ASME 2018 13th International Manufacturing Science and Engineering Conference, American Society of Mechanical Engineers Digital Collection, 2018, p.V001T01A038.
- [9] F. Imani, A. Gaikwad, M. Montazeri, P. Rao, H. Yang, E. Reutzel, Process mapping and in-process monitoring of porosity in laser powder bed fusion using layerwise optical imaging, J. Manuf. Sci. Eng. 140 (10) (2018), 101009.
- [10] B. Yao, F. Imani, H. Yang, Markov decision process for image-guided additive manufacturing, IEEE Robot. Autom. Lett. 3 (4) (2018) 2792–2798.
- [11] B. Yao, H. Yang, Constrained markov decision process modeling for sequential optimization of additive manufacturing build quality, IEEE Access 6 (2018) 54786–54794.
- [12] D. Thomas. The Development of Design Rules for Selective Laser Melting (Ph.D. thesis), University of Wales, 2009.
- [13] A. Dunbar, G. Gunderman, M. Mader, E. Reutzel, Fabrication and quality assessment of thin fins built using metal powder bed fusion additive manufacturing, in: 28th Annual International Solid Freeform Fabrication Symposium An Additve Manufacturing Conference, Austin, TX, University of Texas at Austin, 2017, pp. 2650–2663.
- [14] J. Kranz, D. Herzog, C. Emmelmann, Design guidelines for laser additive manufacturing of lightweight structures in tial6v4, J. Laser Appl. 27 (S1) (2015) S14001.
- [15] A. Gaikwad, F. Imani, H. Yang, E. Reutzel, P. Rao, In-situ monitoring of thin-wall build quality in laser powder bed fusion using deep learning, ASTM Int. J. Smart Sustain. Manuf. Syst. (SSMS) 3 (1) (2019) 98–121.
- [16] R. Chen, F. Imani, E. Reutzel, H. Yang, From design complexity to build quality in additive manufacturinga sensor-based perspective, IEEE Sens. Lett. 3 (1) (2018) 1–4.
- [17] S. Kamarthi, S. Sultornsanee, A. Zeid, Recurrence quantification analysis to estimating surface roughness in finish turning processes, Int. J. Adv. Manuf. Technol. 87 (1–4) (2016) 451–460.
- [18] N. Marwan, M.C. Romano, M. Thiel, J. Kurths, Recurrence plots for the analysis of complex systems, Phys. Rep. 438 (5–6) (2007) 237–329.
- [19] J. Eckmann, S.O. Kamphorst, D. Ruelle, et al., Recurrence plots of dynamical systems, World Sci. Ser. Nonlinear Sci. Ser. A 16 (1995) 441–446.
- [20] H. Yang, G. Liu, Self-organized topology of recurrence-based complex networks, Chaos Interdiscip. J. Nonlinear Sci. 23 (4) (2013), 043116.
- [21] J.P. Zbilut, C.L. Webber Jr, Recurrence quantification analysis: introduction and historical context, Int. J. Bifurc. Chaos 17 (10) (2007) 3477–3481.
- [22] H. Yang, Y. Chen, Heterogeneous recurrence monitoring and control of nonlinear stochastic processes, Chaos Interdiscip. J. Nonlinear Sci. 24 (1) (2014), 013138.
- [23] Y. Chen, H. Yang, Heterogeneous recurrence representation and quantification of dynamic transitions in continuous nonlinear processes, Eur. Phys. J. B 89 (6) (2016) 155.
- [24] C. Kan, C. Cheng, H. Yang, Heterogeneous recurrence monitoring of dynamic transients in ultraprecision machining processes, J. Manuf. Syst. 41 (2016) 178–187.

- [25] C. Cheng, C. Kan, H. Yang, Heterogeneous recurrence analysis of heartbeat dynamics for the identification of sleep apnea events, Comput. Biol. Med. 75 (2016) 10–18.
- [26] R. Chen, F. Imani, H. Yang, Heterogeneous recurrence analysis of disease-altered spatiotemporal patterns in multi-channel cardiac signals, IEEE J. Biomed. Health Inform. 24 (6) (2020) 1619–1631.
- [27] H. Yang, C.-B. Chen, S. Kumara, Heterogeneous recurrence analysis of spatial data, Chaos Interdiscip. J. Nonlinear Sci. 30 (1) (2020), 013119.
- [28] L. Cui, S. Kumara, R. Albert, Complex networks: an engineering view, IEEE Circuits Syst. Mag. 10 (3) (2010) 10–25.
- [29] H.B. Mann, D.R. Whitney, On a test of whether one of two random variables is stochastically larger than the other, Ann. Math. Stat. 18 (1) (1947) 50–60.
- [30] C. Wang, X. Tan, S. Tor, C. Lim, Machine learning in additive manufacturing: state-of-the-art and perspectives, Addit. Manuf. 36 (2020), 101538.
- [31] J. Zhang, P. Wang, R.X. Gao, Attention mechanism-incorporated deep learning for am part quality prediction, Procedia CIRP 93 (2020) 96–101.
- [32] M. Mozaffar, A. Paul, R. Al-Bahrani, S. Wolff, A. Choudhary, A. Agrawal, K. Ehmann, J. Cao, Data-driven prediction of the high-dimensional thermal history

- in directed energy deposition processes via recurrent neural networks, Manuf. Lett. $18\ (2018)\ 35-39$.
- [33] J. Francis, L. Bian, Deep learning for distortion prediction in laser-based additive manufacturing using big data, Manuf. Lett. 20 (2019) 10–14.
- [34] C. Kan, H. Yang, Internet of hearts-large-scale stochastic network modeling and analysis of cardiac electrical signals, in: Stochastic Modeling and Analytics in Healthcare Delivery Systems, World Scientific, 2017, pp. 211–251.
- [35] G. Liu, H. Yang, Self-organizing network for variable clustering, Ann. Oper. Res. 263 (1–2) (2018) 119–140.
- [36] C. Kan, H. Yang, Network models for monitoring high-dimensional image profiles, in: 2015 IEEE International Conference on Automation Science and Engineering (CASE), IEEE, 2015, pp. 1078–1083.
- [37] C.-B. Chen, H. Yang, S. Kumara, Recurrence network modeling and analysis of spatial data, Chaos Interdiscip. J. Nonlinear Sci. 28 (8) (2018), 085714.
- [38] H. Yang, R. Liu, S. Kumara, Self-organizing network modelling of 3d objects, CIRP Ann. 69 (1) (2020) 409–412.